Far beyond the Sun – I. The beating magnetic heart in Horologium

Julián Alvarado-Gómez, Gaitee A. J. Hussain, Jeremy Drake, Jean-François Donati, Jorge Sanz-Forcada, Beate Stelzer, Ofer Cohen, Eliana Amazo-Gómez, Jason Grunhut, Cecilia Garraffo, et al.

Julián Alvarado-Gómez, Gaitee A. J. Hussain, Jeremy Drake, Jean-François Donati, Jorge Sanz-Forcada, et al.. Far beyond the Sun – I. The beating magnetic heart in Horologium. Monthly Notices of the Royal Astronomical Society, 2018, 473 (4), pp.4326-4338. 10.1093/mnras/stx2642 . obspm-02296260

HAL Id: obspm-02296260
https://hal-obspm.ccsd.cnrs.fr/obspm-02296260v1

Submitted on 22 Nov 2024

Monthly Notices
of the
ROYAL ASTRONOMICAL SOCIETY

MNRAS **473,** 4326–4338 (2018)
Advance Access publication 2017 October 10

doi:10.1093/mnras/stx2642

Far beyond the Sun – I. The beating magnetic heart in Horologium

Julián D. Alvarado-Gómez,[1★] Gaitee A. J. Hussain,[2,3] Jeremy J. Drake,[1]
Jean-François Donati,[4] Jorge Sanz-Forcada,[5] Beate Stelzer,[6] Ofer Cohen,[7]
Eliana M. Amazo-Gómez,[8,9] Jason H. Grunhut,[10] Cecilia Garraffo,[1]
Sofia P. Moschou,[1] James Silvester[11] and Mary E. Oksala[12,13]

[1] *Harvard–Smithsonian Center for Astrophysics, 60 Garden Street, Cambridge, MA 02138, USA*
[2] *European Southern Observatory, Karl-Schwarzschild-Str. 2, D-85748 Garching bei München, Germany*
[3] *Institut de Recherche en Astrophysique et Planétologie, Université de Toulouse, UPS-OMP, F-31400 Toulouse, France*
[4] *CNRS-IRAP, 14, avenue Edouard Belin, F-31400 Toulouse, France*
[5] *Centro de Astrobiología (CSIC-INTA), ESAC Campus, Camino Bajo del Castillo, E-28692 Villanueva de la Cañada, Madrid, Spain*
[6] *Institut für Astronomie und Astrophysik, Eberhard Karls Universität, Sand 1, D-72076 Tübingen, Germany*
[7] *Department of Physics and Applied Physics, University of Massachusetts at Lowell, 600 Suffolk St, Lowell, MA 01854, USA*
[8] *Max-Planck-Institut für Sonnensystemforschung, Justus-von-Liebig-Weg 3, D-37077 Göttingen, Germany*
[9] *Institut für Astrophysik, Georg-August Universität Göttingen, Friedrich-Hund-Platz 1, D-37077 Göttingen, Germany*
[10] *Dunlap Institute for Astronomy and Astrophysics, University of Toronto, 50 St George Street, Toronto, ON M5S 3H4, Canada*
[11] *Department of Astronomy and Space Physics, Uppsala University, SE-751 20 Uppsala, Sweden*
[12] *LESIA, Observatoire de Paris, PSL Research University, CNRS, Sorbonne Universités, UPMC, Univ. Paris 6, Univ. Paris Diderot, Sorbonne Paris Cité, 5 place Jules Janssen, F-92195 Meudon, France*
[13] *Department of Physics, California Lutheran University, 60 West Olsen Road #3700, Thousand Oaks, CA 91360, USA*

Accepted 2017 October 6. Received 2017 October 5; in original form 2017 August 2

ABSTRACT

A former member of the Hyades cluster, ι Horologii (ι Hor) is a planet-hosting Sun-like star which displays the shortest coronal activity cycle known to date ($P_{\rm cyc} \sim 1.6$ yr). With an age of ∼625 Myr, ι Hor is also the youngest star with a detected activity cycle. The study of its magnetic properties holds the potential to provide fundamental information to understand the origin of cyclic activity and stellar magnetism in late-type stars. In this series of papers, we present the results of a comprehensive project aimed at studying the evolving magnetic field in this star and how this evolution influences its circumstellar environment. This paper summarizes the first stage of this investigation, with results from a long-term observing campaign of ι Hor using ground-based high-resolution spectropolarimetry. The analysis includes precise measurements of the magnetic activity and radial velocity of the star, and their multiple time-scales of variability. In combination with values reported in the literature, we show that the long-term chromospheric activity evolution of ι Hor follows a beating pattern, caused by the superposition of two periodic signals of similar amplitude at $P_1 \simeq 1.97 \pm 0.02$ yr and $P_2 \simeq 1.41 \pm 0.01$ yr. Additionally, using the most recent parameters for ι Hor b in combination with our activity and radial velocity measurements, we find that stellar activity dominates the radial velocity residuals, making the detection of additional planets in this system challenging. Finally, we report here the first measurements of the surface longitudinal magnetic field strength of ι Hor, which displays varying amplitudes within ±4 G and served to estimate the rotation period of the star ($P_{\rm rot} = 7.70^{+0.18}_{-0.67}$ d).

Key words: techniques: polarimetric – stars: activity – stars: individual: ι Hor – stars: individual: HD 17051 – stars: individual: HR 810 – stars: magnetic field – stars: solar-type.

★ E-mail: julian.alvarado-gomez@cfa.harvard.edu

Published by Oxford University Press on behalf of the Royal Astronomical Society

1 INTRODUCTION

Early studies performed by Wilson (1968), Vaughan & Preston (1980), Baliunas et al. (1995) and Henry et al. (1996) showed that chromospheric emission and activity cycles are a common feature among late-type stars. Cyclic variability of the Ca II H (396.84 nm) & K (393.36 nm) emission cores is observed in about 60 per cent of main-sequence stars in the solar neighbourhood, including spectral types from early M to F (Baliunas et al. 1995). The cycle periods range from 2.5 to 25 yr, placing the ∼11-yr solar activity cycle in the middle of the distribution, and the cycle occurrence rate is related to the mean activity level (and therefore to stellar rotation and age; see Skumanich 1972; Noyes et al. 1984). Recent efforts are being carried out in order to extend the baseline of observations and increase the sample of identified cycles (e.g. Hall, Lockwood & Skiff 2007; Hall et al. 2009; Mauas et al. 2012), and to place the solar chromosphere in the general stellar context (e.g. Egeland et al. 2016; Metcalfe, Egeland & van Saders 2016).

The standard picture for the origin of these stellar activity cycles comes from our knowledge of the behaviour of the Sun's magnetism. It is widely accepted that the 11-yr global activity changes of the Sun appear as a consequence of a 22-yr magnetic cycle which, among other features, is primarily characterized by a double polarity reversal of the small-[1] and large-scale fields (Mackay & Yeates 2012; Hathaway 2015). The latter are nowadays accessible in the stellar case via spectropolarimetric observations and the technique of Zeeman Doppler Imaging (ZDI; Donati et al. 1997; Piskunov & Kochukhov 2002; Hussain et al. 2009). While large-scale polarity reversals have been detected in a handful of objects (see Fares 2016), in only one of them solar-like cyclic behaviour has been reported (61 Cyg A; see Boro Saikia et al. 2016). For the majority of targets, the reversal time-scale is typically very short (∼1–2 yr) and disconnected from the observed variability in the chromospheric activity, showing no resemblance in this regard to the solar case. It is unclear whether these reversals may have any connection with either stellar equivalents of the solar quasi-biennial oscillation (see Bazilevskaya et al. 2014; McIntosh et al. 2015), a different type of magnetism–activity relation in active stars or an observational bias introduced by the methods used in these comparisons. Efforts are still ongoing in order to connect the properties of the recovered magnetic fields with the characteristics of the stellar activity cycles in these systems (see See et al. 2016).

Following the solar analogy, a clearer signature of these stellar chromospheric activity cycles is expected from the coronal high-energy emission (e.g. UV/X-rays). Indeed, the amplitude of the solar chromospheric Ca H&K cycle is only few per cent of the mean value (see Egeland et al. 2017 and references therein), while in coronal X-rays, particularly in the soft X-ray band (i.e. 1–8 Å), cycle amplitudes between 0.7 and 2.0 dex have been reported (Aschwanden 1994; Orlando, Peres & Reale 2001; Judge, Solomon & Ayres 2003). Unfortunately, even in the optimistic scenario of solar-like cycle amplitudes, the detection of stellar X-ray cycles is greatly compromised by the difficulty in maintaining homogeneous (i.e. with the same instrument) and continuous monitoring over cycle time-scales. The increased coverage achieved by combining data sets from different instruments involves non-trivial cross-calibration procedures, which are not only cumbersome but also may introduce dominant spurious signals to the data (e.g. the case of α Cen A; see Ayres et al. 2008).

Table 1. Fundamental properties of ι Hor.

Parameter	Value	Reference
Spectral type	F8V–G0V	Bruntt et al. (2010)
$T_{\rm eff}$ (K)	6080 ± 80	Bruntt et al. (2010)
$\log{(g)}$	4.399 ± 0.022	Bruntt et al. (2010)
R_* ($\mathrm{R}_\odot$)	1.16 ± 0.04	Bruntt et al. (2010)
M_* ($\mathrm{M}_\odot$)	1.23 ± 0.12	Bruntt et al. (2010)
$v\sin i$ (km s^{-1})	6.0 ± 0.5	This work
$\langle v_{\rm R} \rangle$ (km s^{-1})^a	16.943 ± 0.002	This work
$P_{\rm rot}$ (d)	$7.70^{+0.18}_{-0.67}$	This work
$\langle \log{(L_{\rm X})} \rangle$	28.78 ± 0.08	Sanz-Forcada et al. (2013)
Age (Myr)^b	∼625	Vauclair et al. (2008)

Notes. ^{a}Average value from the multi-epoch HARPSpol observations (see Section 3).
^{b}Age derived from HARPS asteroseismology. This value falls in between the estimates from gyrochronology (∼740 Myr; Barnes 2007) and from the level of X-ray/EUV emission (∼500 Myr; Sanz-Forcada et al. 2011).

For these reasons, it is not surprising that X-ray activity cycles have been identified only in five late-type stars.[2] Three members of this group, namely HD 81809 (G2V + G9V, $P_{\rm cyc} = 8.2$ yr; Favata et al. 2004, 2008), 61 Cyg A (K5V, $P_{\rm cyc} = 7.3$ yr; Hempelmann et al. 2006; Robrade, Schmitt & Favata 2012) and α Cen B (K1V, $P_{\rm cyc} = 8.1$ yr; Ayres 2009, 2014; DeWarf, Datin & Guinan 2010; Robrade et al. 2012), belong to binary systems (where non-cycle-related mechanisms could be involved in the X-ray variability). Recently, Wargelin et al. (2017) reported an X-ray activity cycle of $P_{\rm cyc} = 7.1$ yr for the fully convective M-dwarf Proxima Cen (M5.5V), coincident with the long-term photometric variability of the star (Suárez Mascareño, Rebolo & González Hernández 2016). The remaining star in this sample is ι Horologii (HD 17051 = HR 810, G0V), which not only displays the shortest X-ray cycle known to date ($P_{\rm cyc} = 1.6$ yr; Sanz-Forcada, Stelzer & Metcalfe 2013), but is also the youngest star with a detected cycle (∼625 Myr, see Table 1). The 1.6-yr activity cycle of ι Hor was first identified by Metcalfe et al. (2010) in chromospheric emission and, using additional Ca H&K data, Flores et al. (2017) recently suggested the presence of a secondary ∼4.5-yr periodicity. As very young stars show erratic and non-cyclic activity (see Baliunas et al. 1995; Saar & Brandenburg 1999; Katsova, Bondar & Livshits 2015; Oláh et al. 2016), the magnetic and activity cycles of ι Hor could be representative of the onset of cycles during the life of a Sun-like star and provide critical information to understand the generation and evolution of magnetism in late-type stars.

In this context, this paper is the first in a series of articles containing the results of the '*Far beyond the Sun*' campaign: an observational–numerical study aimed at characterizing the magnetic cycle of ι Hor using high-resolution spectropolarimetry, and determining (from data-driven simulations), how this evolving field influences the corona and wind environment around the star. Here, we introduce the observing programme and focus on the different time-scales of variability of the activity indicators, the radial velocity (RV) of the star and the surface-averaged longitudinal magnetic field. The astrophysical properties of ι Hor are presented in Section 2. Section 3 contains a description of the observations and data processing. A description of the different measurements and

---

[1] The terms small and large are used here in the stellar context; the former indicates spots/active region size while the latter is used for the star as a whole.

[2] Possibly six if the tentative ∼19-yr cycle of α Cen A is confirmed (Ayres 2014).

their results is provided in Section 4. We analyse and discuss our findings in Section 5, and summarize our work in Section 6.

2 ASTROPHYSICAL PROPERTIES OF ι HOR

The 11th brightest star of the Horologium constellation (the pendulum clock), ι Hor ($V_{\mathrm{mag}} = 5.4$) is a young Sun-like star located at 17.17 ± 0.06 pc from the Sun (van Leeuwen 2007). Despite its location in the Southern hemisphere [α (J2000): $02^{\mathrm{h}}42^{\mathrm{m}}33\overset{\mathrm{s}}{.}47$, δ (J2000): $-50^{\circ}48'01\overset{\prime\prime}{.}10$], strong evidence suggests that the star was formed in the Hyades cluster, currently sharing the same kinematic properties (i.e. part of the Hyades stream; Montes et al. 2001; Nordström et al. 2004), and having the same metallicity, helium abundance and age (Laymand & Vauclair 2007; Vauclair et al. 2008).

The star is also known to host an ∼2.5 Jupiter-mass planet at approximately 1 au. The exoplanet was discovered by Kürster et al. (2000), and shortly after confirmed independently by Naef et al. (2001) and Butler et al. (2001). The most recent orbital parameters of this system ($M_{\mathrm{p}}\sin(i) = 2.48 \pm 0.08$ M$_{\mathrm{J}}$, $P_{\mathrm{orb}} = 307.2 \pm 0.3$ d, $e = 0.18 \pm 0.03$, $a = 0.96 \pm 0.05$ au) were obtained by Zechmeister et al. (2013) using a compilation of RVs from all previous studies (including additional data presented by Butler et al. 2006), together with new RV measurements from *ESO*'s CES and HARPS spectrographs. The combined solution reproduces the ∼15-yr baseline of RV measurements, although relatively high scatter is obtained in the orbit residuals (with an rms of 14.5 m s^{-1}). Zechmeister et al. (2013) acknowledge the presence of an activity cycle of ι Hor, which shows a roughly 2:1 relation with the orbital period of the planet. Nevertheless, they conclude that the activity cycle is not responsible for the observed RV signal, although it can certainly be the dominant cause for the scatter in the residuals, particularly, since the activity-filtering analysis of Boisse et al. (2011) ruled out companions with orbital periods shorter than 7 d.

Table 1 contains a summary of the main properties of ι Hor and their corresponding references. Using the fundamental parameters provided by Bruntt et al. (2010) and applying a standard spectral synthesis on a set of iron Fe I and Fe II lines under Kurucz ATLAS9 model atmospheres in local thermodynamic equilibrium, we obtained a projected rotational velocity of 6.0 ± 0.5 km s^{-1}. This result is consistent with the value reported by Valenti & Fischer (2005) derived from a similar analysis based on UCLES@AAT spectra (Diego et al. 1990). As discussed in more detail in the next section, we measure the RV on each night and calculate the long-term average $\langle v_{\mathrm{R}}\rangle$ listed in Table 1. Likewise, our analysis indicates a rotation period of $P_{\mathrm{rot}} = 7.70^{+0.18}_{-0.67}$ d, roughly consistent with previous reports from Saar & Osten (1997) and Metcalfe et al. (2010), estimated using different methods (see Section 5.3).

3 OBSERVATIONS AND DATA PROCESSING

3.1 Spectropolarimetric data

3.1.1 *Observing strategy*

We began the monitoring of the magnetic cycle of ι Hor in 2015 October, using the spectropolarimetric mode of the HARPS spectrograph (HARPSpol) attached at the *ESO* 3.6 m telescope located at the La Silla Observatory in Chile (Mayor et al. 2003; Piskunov et al. 2011).

Apart from seasonal visibility, two important elements determined the observing strategy for this programme. The first one considered the coverage needed in order to resolve the expected activity cycle evolution, taking the results from the ongoing X-ray monitoring of the star as reference (Sanz-Forcada & Stelzer 2016). On the other hand, for each observing epoch, we required sufficient (rotational) phase sampling to guarantee the successful retrieval of the magnetic field distributions using ZDI[3] (including possible weather losses). Given the moderate activity levels of ι Hor (i.e. Ca H&K *S*-index between 0.23 and 0.28), and the large amount of telescope time required for a single full Stokes ZDI inversion (even for stars with stronger magnetic fields; see Rosén, Kochukhov & Wade 2015), only circular polarization (Stokes *V*) was considered.

The exposure time requirements were based on our previous HARPSpol experience mapping magnetic fields of stars with similar activity levels and spectral type (e.g. Alvarado-Gómez et al. 2015; Hussain et al. 2016). To achieve the required S/N (∼400–500@550 nm) and to prevent any possible saturation of the detector (taking into account the visual brightness of the star; see Section 2), the acquisition of two (or three) Stokes *V* exposures consecutively during the same night was planned, with a total integration time of ∼ 1 h per night.[4] In this way, nine epochs have been secured over an ∼1.4-yr baseline (between 2015 October and 2017 February). One epoch consists of roughly two weeks of almost consecutive nights, each one of these composed of 1–3 high S/N merged Stokes *V* exposures (effectively 4–12 spectra per night) which, as described below, also yield extremely high S/N unpolarized spectra (Stokes *I*). Details for the individual nights can be found in the journal of observations (columns 1–5 of Table 2).

3.1.2 *Level 1 processing*

The retrieval of the circularly polarized spectra is performed using the ratio method (see Donati et al. 1997; Bagnulo et al. 2009). Four subexposures, each one consisting of two orthogonal polarization states (carried separately by individual fibres to the spectrograph), are divided coherently to produce a single Stokes *V* spectrum. By considering a ratio, an effective first-order removal of spurious signals and systematic errors is automatically performed. This is complemented with the aid of the so-called null polarization spectrum (denoted by N), generated from the ratio of destructive (incoherent) polarization states. By construction, the N spectrum should remain at the zero level at all times if only polarization from the astrophysical object is considered (deviations from zero are indicative of spurious signals). The Stokes *I* spectra are generated by simply co-adding all the subexposures together, which typically leads to much larger S/N than in standard spectroscopic stellar observations.

The data reduction process was carried out using the automatic LIBRE-ESPRIT package (see Donati et al. 1997), which has been recently modified to handle the extraction of HARPSpol observations, preserving the standard RV precision of the instrument (cf. Hébrard et al. 2016; Hussain et al. 2016). The spectra are obtained following an optimal extraction scheme, after bias, flat-field and cosmic ray corrections are applied. Two different sets of ThAr arc spectra are used to compute the wavelength solution and the corresponding barycentric corrections for each night. The latter are obtained from

---

[3] The recovered ZDI large-scale magnetic field maps for each epoch will be presented in the second paper of this study.

[4] Owing to bad weather conditions, on four separate nights only a single Stokes *V* exposure was retrieved (see Table 2). Likewise, rapidly changing weather during the night of 2016 September 13 (BJD: 2457646.77036) required the acquisition of four Stokes *V* exposures to secure the required S/N level.

Table 2. Journal of observations (columns 1–5) and measurements for each night (columns 6–11).

	BJD (+2400000.) (d)	# Exp.[a]	S/N [@551 nm]		v_{r} (m s^{-1})	Activity indicators		B_ℓ (G)	N_ℓ (G)	σ_ℓ (G)
			I	V		S_{H}	$I_{\mathrm{H}\alpha}$			
(2015 October)	57300.78580	2	677	657	16 887.00 ± 2.53	0.2315 ± 0.0056	0.5115 ± 0.0014	2.23	0.05	0.41
	57301.78847	1	241	222	16 889.58 ± 4.41	0.2281 ± 0.0190	0.5127 ± 0.0039	1.52	3.05	1.23
	57302.78891	2	559	535	16 907.38 ± 2.68	0.2486 ± 0.0072	0.5124 ± 0.0017	0.21	0.01	0.49
	57303.79205	2	849	810	16 903.73 ± 2.33	0.2442 ± 0.0046	0.5140 ± 0.0011	− 0.46	− 0.01	0.32
	57304.78161	2	306	230	16 914.80 ± 3.82	0.2318 ± 0.0138	0.5118 ± 0.0032	0.58	0.70	1.16
	57305.78524	2	648	617	16 894.02 ± 2.67	0.2460 ± 0.0062	0.5123 ± 0.0015	0.92	0.04	0.42
	57306.78315	2	814	771	16 898.14 ± 2.41	0.2372 ± 0.0050	0.5124 ± 0.0012	− 2.29	0.32	0.33
	57307.77570	2	726	709	16 910.59 ± 2.40	0.2355 ± 0.0054	0.5118 ± 0.0013	− 1.64	0.11	0.37
	57308.78898	1	442	425	16 899.08 ± 3.21	0.2401 ± 0.0092	0.5127 ± 0.0021	1.99	− 0.49	0.62
	57311.78572	2	922	899	16 917.38 ± 2.26	0.2449 ± 0.0043	0.5138 ± 0.0010	− 1.30	− 0.18	0.29
	57312.76899	2	778	752	16 914.48 ± 2.35	0.2460 ± 0.0050	0.5141 ± 0.0012	0.48	0.32	0.35
(2015 December)	57374.55060	2	1068	1025	16 997.89 ± 2.12	0.2462 ± 0.0036	0.5149 ± 0.0009	− 0.07	− 0.71	0.26
	57375.54055	2	811	769	16 966.98 ± 2.39	0.2461 ± 0.0047	0.5150 ± 0.0012	− 0.23	0.35	0.33
	57379.55264	2	1159	1108	17 000.88 ± 1.98	0.2388 ± 0.0035	0.5136 ± 0.0008	1.55	0.62	0.23
	57380.55509	2	1005	964	16 994.96 ± 2.15	0.2430 ± 0.0039	0.5140 ± 0.0009	3.98	− 0.01	0.27
	57381.55544	2	1090	1038	16 994.17 ± 2.12	0.2435 ± 0.0036	0.5141 ± 0.0009	3.00	0.14	0.25
	57382.55338	2	1010	950	16 993.68 ± 2.12	0.2439 ± 0.0039	0.5139 ± 0.0010	2.26	0.44	0.27
	57383.55427	2	1214	1136	16 969.50 ± 1.96	0.2403 ± 0.0034	0.5131 ± 0.0008	− 0.19	− 0.06	0.22
	57384.55438	2	1141	1071	16 996.00 ± 2.04	0.2439 ± 0.0036	0.5129 ± 0.0008	− 1.58	0.24	0.24
	57385.55417	2	1036	986	17 009.91 ± 2.03	0.2464 ± 0.0038	0.5133 ± 0.0009	− 1.37	0.33	0.26
	57386.54757	2	1100	1062	17 002.64 ± 2.04	0.2452 ± 0.0036	0.5135 ± 0.0009	− 0.37	0.13	0.24
	57387.56851	2	1083	1039	17 013.08 ± 2.01	0.2504 ± 0.0040	0.5138 ± 0.0009	2.03	0.48	0.25
(2016 February)	57436.54183	3	1156	1106	16 982.76 ± 2.03	0.2522 ± 0.0042	0.5148 ± 0.0008	− 0.58	− 0.09	0.25
	57437.53818	3	1306	1257	16 970.25 ± 1.85	0.2540 ± 0.0039	0.5146 ± 0.0007	− 0.21	− 0.10	0.21
	57438.55301	3	1112	1060	16 967.33 ± 2.09	0.2472 ± 0.0043	0.5147 ± 0.0008	0.91	− 0.14	0.25
	57439.54492	3	1192	1157	16 995.00 ± 1.94	0.2470 ± 0.0041	0.5139 ± 0.0008	1.49	− 0.00	0.23
	57440.54027	3	1332	1276	16 950.56 ± 1.82	0.2516 ± 0.0039	0.5132 ± 0.0007	1.39	0.01	0.21
	57441.53922	3	1040	996	16 931.62 ± 2.22	0.2465 ± 0.0048	0.5126 ± 0.0009	0.08	− 0.31	0.27
	57442.54183	3	964	929	16 954.12 ± 2.16	0.2413 ± 0.0052	0.5109 ± 0.0009	0.81	− 0.01	0.29
	57444.54762	2	357	345	16 937.70 ± 3.66	0.2604 ± 0.0126	0.5121 ± 0.0027	− 0.51	− 0.06	0.76
	57445.53731	3	975	958	16 947.29 ± 2.15	0.2471 ± 0.0047	0.5120 ± 0.0010	− 0.50	− 0.24	0.28
(2016 June)	57562.92231	3	886	857	16 899.33 ± 2.24	0.2420 ± 0.0043	0.5133 ± 0.0011	0.62	0.01	0.31
	57567.92469	2	880	857	16 887.04 ± 2.20	0.2396 ± 0.0044	0.5129 ± 0.0011	2.07	0.36	0.31
	57568.92232	2	749	712	16 878.23 ± 2.53	0.2382 ± 0.0053	0.5124 ± 0.0013	1.21	0.51	0.36
	57569.92692	2	830	806	16 893.89 ± 2.30	0.2441 ± 0.0045	0.5118 ± 0.0012	− 1.10	− 0.10	0.32
	57570.91827	2	852	825	16 884.99 ± 2.32	0.2427 ± 0.0045	0.5126 ± 0.0011	0.06	0.05	0.32
	57575.92260	2	690	671	16 883.47 ± 2.54	0.2461 ± 0.0056	0.5138 ± 0.0014	0.67	0.35	0.39
	57576.92258	2	738	706	16 881.69 ± 2.55	0.2444 ± 0.0053	0.5130 ± 0.0013	0.05	− 0.35	0.37
	57589.85636	3	889	861	16 895.13 ± 2.29	0.2388 ± 0.0043	0.5117 ± 0.0011	1.06	− 0.11	0.30
(2016 August)	57619.81856	2	618	593	16 905.42 ± 2.80	0.2472 ± 0.0063	0.5139 ± 0.0015	− 0.97	− 0.02	0.45
	57621.82170	2	719	693	16 899.17 ± 2.49	0.2396 ± 0.0053	0.5137 ± 0.0013	0.26	0.31	0.37
	57622.83422	2	781	751	16 905.58 ± 2.48	0.2397 ± 0.0049	0.5135 ± 0.0012	0.54	0.51	0.34
	57623.81619	2	955	929	16 914.81 ± 2.12	0.2402 ± 0.0041	0.5128 ± 0.0010	0.70	0.09	0.28
	57624.82099	2	784	753	16 908.49 ± 2.43	0.2427 ± 0.0050	0.5139 ± 0.0012	0.97	− 0.80	0.35
	57625.82139	2	977	941	16 937.99 ± 2.20	0.2457 ± 0.0040	0.5141 ± 0.0010	2.16	0.38	0.27
	57626.86328	2	566	538	16 928.33 ± 2.81	0.2489 ± 0.0064	0.5151 ± 0.0017	0.79	0.00	0.47
	57629.81840	2	862	856	16 905.51 ± 2.23	0.2428 ± 0.0044	0.5130 ± 0.0011	− 0.16	− 0.17	0.31
	57630.82050	2	974	929	16 919.88 ± 2.18	0.2419 ± 0.0039	0.5135 ± 0.0010	− 0.30	− 0.05	0.27
	57631.81518	2	1118	1069	16 921.00 ± 1.98	0.2441 ± 0.0035	0.5133 ± 0.0009	0.28	− 0.03	0.24
	57632.81974	2	904	868	16 914.84 ± 2.29	0.2435 ± 0.0043	0.5141 ± 0.0011	0.48	− 0.27	0.30
(2016 Sep.)	57645.79605	4	948	916	16 981.41 ± 2.25	0.2467 ± 0.0040	0.5144 ± 0.0010	0.79	0.02	0.29
	57646.77036	2	739	678	16 949.99 ± 2.40	0.2465 ± 0.0050	0.5134 ± 0.0013	0.06	0.38	0.38
	57647.78723	2	1107	1081	16 947.88 ± 1.96	0.2459 ± 0.0035	0.5131 ± 0.0009	− 0.08	0.36	0.24
	57648.81725	2	998	961	16 945.52 ± 2.03	0.2522 ± 0.0038	0.5134 ± 0.0010	3.00	0.12	0.27
	57649.84913	2	735	707	16 935.93 ± 2.47	0.2509 ± 0.0049	0.5140 ± 0.0013	3.24	0.14	0.36
	57650.85027	2	1092	1032	16 921.65 ± 2.01	0.2458 ± 0.0037	0.5142 ± 0.0009	1.17	0.07	0.25
	57651.84535	2	953	924	16 952.32 ± 2.16	0.2442 ± 0.0041	0.5136 ± 0.0010	− 0.41	0.08	0.28
	57652.85980	2	1037	996	16 948.99 ± 1.93	0.2465 ± 0.0039	0.5137 ± 0.0009	0.50	0.38	0.26
	57654.84500	3	790	771	16 958.12 ± 2.34	0.2421 ± 0.0049	0.5132 ± 0.0012	− 1.38	− 0.12	0.34
	57655.86385	3	1133	1094	16 974.67 ± 1.96	0.2453 ± 0.0039	0.5132 ± 0.0008	0.98	− 0.16	0.24
	57656.80459	2	1073	1051	16 946.08 ± 2.00	0.2475 ± 0.0037	0.5144 ± 0.0009	1.88	0.00	0.25
	57657.84229	2	960	928	16 939.42 ± 2.10	0.2531 ± 0.0047	0.5146 ± 0.0010	2.53	0.09	0.29
	57658.82478	2	1117	1071	16 947.05 ± 2.02	0.2483 ± 0.0037	0.5142 ± 0.0009	− 0.56	0.51	0.24
	57659.82063	2	841	796	16 973.45 ± 2.25	0.2470 ± 0.0045	0.5139 ± 0.0012	− 2.00	− 0.10	0.32
(2016 Oct.)	57676.78694	2	595	576	16 980.22 ± 2.76	0.2520 ± 0.0072	0.5129 ± 0.0016	2.09	1.28	0.48

Table 2 – *continued*

	BJD (+2400000.)	# Exp.^{c}	S/N [@551 nm]		v_r	Activity indicators		B_ℓ	N_ℓ	σ_ℓ
	(d)		I	V	(m s^{-1})	S_H	$I_{H\alpha}$	(G)	(G)	(G)
	57679.83434	1	330	310	16 945.60 ± 3.87	0.2418 ± 0.0129	0.5138 ± 0.0029	− 0.14	2.29	0.84
	57680.81105	2	506	500	16 962.62 ± 2.97	0.2355 ± 0.0079	0.5135 ± 0.0019	1.70	1.00	0.53
	57681.79977	2	825	787	16 974.86 ± 2.40	0.2462 ± 0.0051	0.5136 ± 0.0011	− 1.45	0.10	0.33
	57682.81243	2	1015	979	16 993.23 ± 2.07	0.2448 ± 0.0043	0.5143 ± 0.0009	0.60	− 0.22	0.27
	57683.78929	1	398	377	16 962.76 ± 3.40	0.2456 ± 0.0102	0.5135 ± 0.0024	0.60	0.20	0.69
	57684.75537	2	618	588	16 983.77 ± 2.76	0.2449 ± 0.0063	0.5141 ± 0.0015	1.83	− 0.04	0.44
	57686.73238	2	582	564	16 986.12 ± 2.79	0.2463 ± 0.0067	0.5146 ± 0.0016	2.39	0.52	0.46
	57687.78773	2	754	769	16 972.72 ± 2.50	0.2440 ± 0.0053	0.5143 ± 0.0012	2.24	0.02	0.35
	57688.78882	2	921	870	16 970.63 ± 2.28	0.2418 ± 0.0047	0.5138 ± 0.0010	− 0.37	0.08	0.30
	57689.79347	2	848	811	16 983.95 ± 2.38	0.2430 ± 0.0053	0.5141 ± 0.0011	0.00	− 0.09	0.33
(2016 December)	57737.64577	2	901	864	16 968.45 ± 2.33	0.2504 ± 0.0049	0.5128 ± 0.0010	− 2.39	− 0.06	0.48
	57740.65620	2	1009	970	16 968.99 ± 2.14	0.2528 ± 0.0046	0.5152 ± 0.0009	− 0.22	− 0.41	0.27
	57741.67881	2	1002	966	16 961.69 ± 2.17	0.2500 ± 0.0048	0.5150 ± 0.0009	0.62	− 0.32	0.28
	57742.66953	2	1018	968	16 967.62 ± 2.11	0.2547 ± 0.0048	0.5150 ± 0.0009	1.83	− 0.20	0.27
	57743.67149	2	984	938	16 949.96 ± 2.20	0.2535 ± 0.0046	0.5152 ± 0.0010	1.95	0.27	0.28
	57744.64682	2	978	938	16 956.08 ± 2.17	0.2510 ± 0.0045	0.5147 ± 0.0010	− 0.62	0.13	0.28
	57745.65298	2	441	373	16 966.66 ± 3.28	0.2409 ± 0.0106	0.5140 ± 0.0022	− 3.25	0.22	0.71
	57746.66875	2	1074	1039	16 965.44 ± 2.00	0.2547 ± 0.0047	0.5138 ± 0.0009	− 2.79	0.29	0.26
	57747.66166	2	899	876	16 953.07 ± 2.33	0.2579 ± 0.0053	0.5151 ± 0.0010	− 1.81	− 0.04	0.31
	57748.66862	2	561	539	16 956.91 ± 2.89	0.2510 ± 0.0076	0.5144 ± 0.0017	0.17	0.26	0.49
	57749.67434	2	680	658	16 941.97 ± 2.56	0.1827 ± 0.0347	0.5147 ± 0.0013	− 0.81	0.04	0.49
	57750.66759	2	823	784	16 942.47 ± 2.36	0.2527 ± 0.0054	0.5142 ± 0.0011	1.77	− 0.47	0.34
(2017 February)	57781.56521	2	711	680	16 897.54 ± 2.67	0.2479 ± 0.0064	0.5130 ± 0.0013	2.05	0.57	0.40
	57782.57006	2	705	662	16 904.26 ± 2.62	0.2429 ± 0.0064	0.5134 ± 0.0013	0.89	0.04	0.39
	57783.56522	2	932	880	16 901.47 ± 2.22	0.2499 ± 0.0053	0.5128 ± 0.0010	− 3.33	− 0.20	0.31
	57784.56808	2	778	751	16 910.32 ± 2.48	0.2446 ± 0.0058	0.5135 ± 0.0012	− 3.88	0.11	0.36
	57786.56736	2	996	941	16 889.40 ± 2.20	0.2402 ± 0.0052	0.5129 ± 0.0009	− 0.93	− 0.25	0.28
	57789.54820	2	835	789	16 873.32 ± 2.50	0.2470 ± 0.0056	0.5144 ± 0.0011	1.54	0.09	0.33
	57790.54995	2	931	898	16 893.70 ± 2.29	0.2445 ± 0.0050	0.5130 ± 0.0010	1.85	− 0.17	0.30
	57791.55658	2	848	812	16 895.03 ± 2.35	0.2438 ± 0.0054	0.5139 ± 0.0011	− 2.06	0.37	0.33
	57793.56295	2	921	883	16 914.98 ± 2.18	0.2441 ± 0.0054	0.5141 ± 0.0010	− 0.24	− 0.13	0.30
	57794.56707	2	852	810	16 896.89 ± 2.35	0.2444 ± 0.0056	0.5145 ± 0.0011	− 0.86	0.05	0.33
	57795.56821	2	706	673	16 920.12 ± 2.71	0.2462 ± 0.0065	0.5145 ± 0.0013	− 1.35	0.22	0.39
	57796.56822	2	993	925	16 904.89 ± 2.07	0.2450 ± 0.0052	0.5140 ± 0.0009	− 1.15	− 0.05	0.28
	57797.56245	2	1071	1023	16 878.10 ± 2.18	0.2430 ± 0.0049	0.5130 ± 0.0009	1.98	0.23	0.26
	57798.57220	2	921	879	16 896.94 ± 2.25	0.2423 ± 0.0055	0.5127 ± 0.0010	0.21	0.07	0.31

Note. ^{a}Number of Stokes V exposures used in the analysis.

the JPL Horizons ephemeris data base,[5] using the information on the stellar exposures and computing the velocity of the observer (and the corresponding time shift) with respect to the barycentre of the Solar system. The pipeline applies a raw automatic continuum normalization over the entire spectral range (378–691 nm), yielding a typical 10 per cent error of the continuum level. This was drastically improved with the aid of two additional procedures. First, a refined continuum shape and normalization were determined using the automatic spline fitting algorithm implemented in the ISPEC package (Blanco-Cuaresma et al. 2014b), with the recommended settings for the HARPS spectrograph (one cubic spline per every nanometre, $R \sim 115\,000$). A second renormalization procedure was then applied by visually inspecting each spectrum over 15 nm windows, and fitting an additional cubic-spline slowly varying envelope to the entire wavelength range. In this way, we achieved a typical error of roughly 1 per cent for the continuum determination in the final reduced spectra.

3.1.3 *Level 2 processing*

The second step in the data processing corresponds to the extraction of the Zeeman signatures from the polarized spectra. As discussed in detail by Donati & Landstreet (2009), the Zeeman components induced by surface magnetic fields in Sun-like stars such as ι Hor are not detectable in individual spectral lines with current instrumentation. The limitation is circumvented with the aid of a multiline cross-correlation technique known as least-squares deconvolution (LSD; see Donati et al. 1997; Kochukhov, Makaganiuk & Piskunov 2010). This technique adds coherently the polarimetric signature from a large number of spectral lines contained in the echelle spectra, and synthesizes extremely high S/N average line profiles (denoted as LSD profiles) for all the relevant polarimetric quantities in each observation (i.e. Stokes I, Stokes V and N spectra).

A photospheric model of the target star (line mask), containing information regarding the rest wavelengths, Landé factors and depths of all the atomic lines within the observed wavelength range, is required to perform the LSD analysis. This was generated using the Vienna Atomic Line Database (VALD3;[6] Kupka et al. 2000; Ryabchikova et al. 2015), assuming a detection threshold of 0.05 (in normalized units), a microturbulence of 1.04 km s^{-1} (Bruntt et al. 2010), together with the $T_{\rm eff}$ and log (g) values listed in Table 1. This line mask was optimized following the methodology presented in Alvarado-Gómez et al. (2015), to closely match

---

[5] https://ssd.jpl.nasa.gov

[6] http://vald.astro.uu.se

all the individual line depths in the observed spectrum. The final mask employed for the extraction of the LSD profiles of ι Hor contains 8834 spectral lines in total. The profiles were extracted for the velocity space between -5.0 and $45.4\,\mathrm{km\,s^{-1}}$, with a velocity step of $\Delta v = 0.8\,\mathrm{km\,s^{-1}}$.

3.2 Archival data

For the analysis presented here, we also used pipeline-processed spectroscopic HARPS archival data,[7] acquired between 2003 November and 2016 December. From all the available observations (2046), we considered only the highest S/N spectrum acquired during each night, which led to a total of 60 additional standard spectra (i.e. not in the polarimetric mode). The phase 3 (PH3) data, which correspond to the final data science products of the *ESO* archive, are fully reduced but no continuum normalization is applied. Therefore, we followed the same two-step normalization procedure as with the spectropolarimetric observations, described in the second part of Section 3.1.2.

4 RESULTS

4.1 RV measurements

In each individual night, we used the extracted LSD Stokes I profile to measure the RV of the star (v_{r}), by considering the resulting centroid from a least-squares Gaussian fit to the data (cf. Marsden et al. 2014; Hébrard et al. 2016). As a consistency check, we measure v_{r} in a couple of spectra per epoch with ISPEC using the default fitting procedure of the cross-correlation function, derived from the provided HARPS/SOPHIE G2 customized line mask (Blanco-Cuaresma et al. 2014a). Both procedures led to very similar results and indicated a typical RV error of $\sim$2 m s^{-1}, as expected for HARPS measurements of an F8V-G0V star with $v\sin(i) \simeq 6.5\,\mathrm{km\,s^{-1}}$ (Lovis & Fischer 2010).

4.2 Magnetic activity indicators

Measurements of two different magnetic activity indicators were performed. The first one corresponds to the HARPS chromospheric S-index (S_{H}), defined by the ratio

$$S_{\mathrm{H}} = \alpha\left(\frac{H+K}{R+V}\right). \quad (1)$$

In this expression, H and K represent the fluxes measured in 0.105 nm bandpasses, centred at the line cores of the Ca II H&K lines (located at 396.8492 and 393.3682 nm, respectively). Similarly, R and V correspond to the integrated fluxes in two nearby continuum regions spanning 2 nm, and centred at 390.107 and 400.107 nm, respectively. To convert S_{H} to the classical Mt. Wilson scale, we used the conversion factor $\alpha = 15.39 \pm 0.65$, previously determined by Alvarado-Gómez et al. (2015).

The second activity indicator considered is the Hα-index ($I_{\mathrm{H}\alpha}$), obtained from the line-to-continuum flux ratio

$$I_{\mathrm{H}\alpha} = \frac{F_{\mathrm{H}\alpha}}{C_{\mathrm{B}} + C_{\mathrm{R}}}. \quad (2)$$

Similar to the S-index, $F_{\mathrm{H}\alpha}$ denotes the flux integrated in a 0.36 nm bandpass around the Hα line core (at 656.2801 nm), while C_{B} and C_{R} are the fluxes in two 0.22 nm pseudo-continuum regions, with central wavelengths located towards the blue (655.885 nm) and red (656.730 nm) of the Hα line (cf. Gizis, Reid & Hawley 2002; Marsden et al. 2014). Similar definitions for $I_{\mathrm{H}\alpha}$ have been employed in previous activity-RV studies of M-dwarf stars, using narrower bandpasses for the line core and continuum flux integration (e.g. Kürster et al. 2003; Bonfils et al. 2007).

4.3 Longitudinal magnetic field

Unlike the activity indicators discussed in the previous section, measurements of the surface-averaged longitudinal magnetic field (B_ℓ) are performed using the results of the LSD analysis (Section 3.1.3). For a pair of LSD Stokes $I(v)$ and $V(v)$ profiles, B_ℓ can be estimated (in gauss) from the following expression (Donati et al. 1997; Donati & Landstreet 2009):

$$B_\ell = -714\frac{\int vV(v)\mathrm{d}v}{\lambda_0\bar{g}\int[I_{\mathrm{c}} - I(v)]\,\mathrm{d}v}. \quad (3)$$

Here, v is the velocity coordinate (in units of km s^{-1}) and I_{c} represents the continuum intensity (in normalized units). The remaining parameters correspond to the central wavelength ($\lambda_0 \simeq 0.509\,\mu\mathrm{m}$) and mean Landé factor ($\bar{g} \simeq 1.198$) of the extracted LSD Stokes I profiles. The uncertainties derived from the spectra through the LSD procedure are propagated to estimate the errors in B_ℓ. However, as discussed by Marsden et al. (2014), additional errors arise from the integration limits used in equation (3). These need to be wide enough to cover the entire profiles, without overextending into the noise-dominated continuum. Therefore, we adopted a velocity range between 5.4 and $30.2\,\mathrm{km\,s^{-1}}$, which maximizes the B_ℓ/σ_ℓ ratio, with σ_ℓ as the final error of the measurement.

Finally, similar measurements (denoted as N_ℓ) are performed by replacing $V(v)$ in equation (3) for the LSD $N(v)$ profiles. This quantity provides a first-order indication of whether B_ℓ may have contributions from spurious polarization (i.e. when $N_\ell > 3\sigma_\ell$). Values of $N_\ell \simeq 0$ are expected (see Section 3.1.2) and typically correspond to robust B_ℓ measurements. However, as these are integrated quantities it is necessary to visually inspect the LSD Stokes $V(v)$ and $N(v)$ profiles, since it is possible to obtain null measurements of either B_ℓ or N_ℓ from profiles where a clear signature is visible.

The resulting values of B_ℓ, N_ℓ and σ_ℓ, as well as the measurements described in Sections 4.1 and 4.2, are listed in Table 2 (columns 6–11).

5 ANALYSIS AND DISCUSSION

5.1 Evolution of the activity: multiple cycles?

The first part of the analysis considers the long-term evolution in the activity levels of ι Hor. We will focus our discussion on the Ca H&K indicator, as the Hα index follows a very similar trend (albeit with a much lesser degree of variability), and there are no previous reports in the literature of the $I_{\mathrm{H}\alpha}$ indicator for this particular star.

Fig. 1 shows our S-index measurements, extracted from the HARPS PH3 (Section 3.2) and HARPSpol data sets, alongside values previously reported by Metcalfe et al. (2010), Sanz-Forcada et al. (2013) and Flores et al. (2017). The former two data sets served to identify the 1.6-yr activity cycle, while the latter[8] was

---

[7] http://archive.eso.org/wdb/wdb/adp/phase3_main/form

[8] The analysis of Flores et al. (2017) also considered monthly averages derived from HARPS archival data. Those values are not included in Fig. 1.

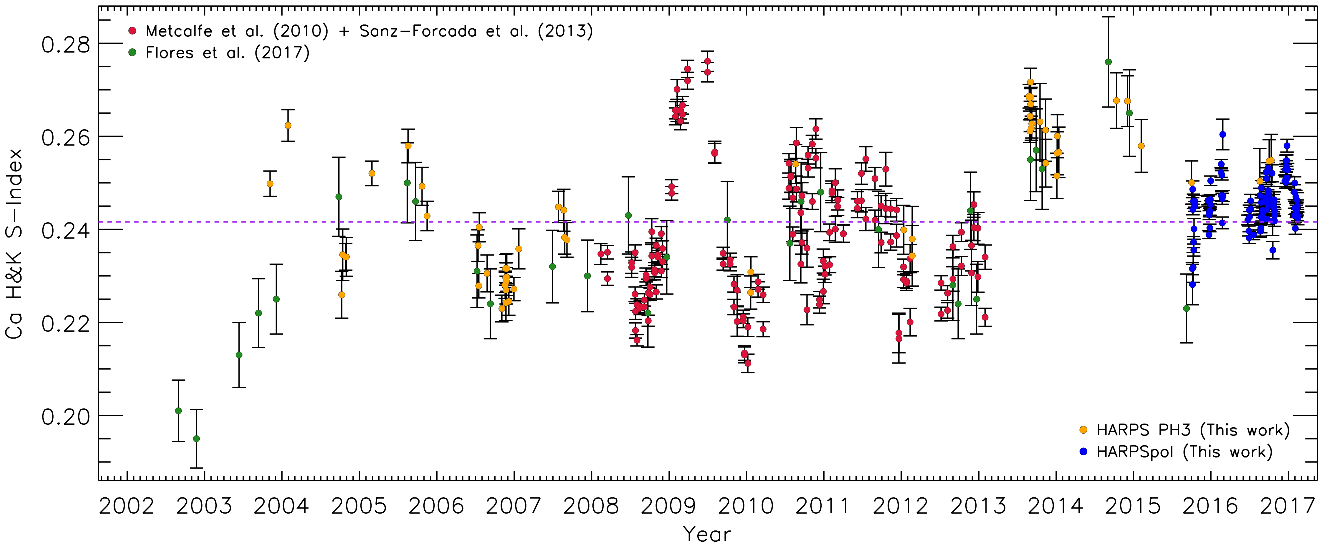

Figure 1. Long-term evolution of the chromospheric Ca H&K S-Index of ι Hor.

used to obtain a secondary period of ∼4.5 yr. By considering the combined data set, it is clear that the activity cycles of ι Hor are relatively irregular and have episodes where no obvious periodicity is visible in the data.

As shown in the figure, our HARPS PH3 S-index values closely follow the previously reported contemporaneous measurements, which were obtained using two different instruments with very dissimilar spectral resolutions: RC Spec ($R \sim 2500$) in the case of Metcalfe et al. (2010) and Sanz-Forcada et al. (2013), and REOSC ($R \sim 26400$) in the case of Flores et al. (2017). This indicates that our HARPS calibration to the Mt. Wilson scale is robust, and gives confidence to the $S_{\rm H}$ values determined at times where no additional observations are available (i.e. the HARPSpol epochs).

Even though our 101 new data points from HARPSpol significantly increase the number of available S-index measurements, their ∼1.4-yr time-span is not sufficient to consider them alone for cycle determination purposes. For this reason, we used the combined data set, consisting of 334 individual measurements spanning ∼14 yr, to check for periodic signals via the classical Lomb–Scargle (LS) periodogram analysis (Lomb 1976; Scargle 1982).

Fig. 2(a) contains the resulting LS periodogram for the combined time series shown in Fig. 1, following the power definition given by Horne & Baliunas (1986). The periods (P_1, P_2, P_3) corresponding to the three most prominent peaks are presented. The associated false alarm probabilities (FAP) have been estimated using a standard bootstrapping randomization algorithm (Bieber et al. 1990), employing 10^5 synthetic periodograms (preserving the time-spacing of the data points). While the 1.6-yr (∼584 d) periodicity could possibly be associated with the third identified peak ($P_3 = 572.73$ d), the first peak located at $P_1 = 726.66$ d has a much lower FAP (by two orders of magnitude). Still, the amplitudes of both of these peaks are comparable, indicating a similar contribution to the periodicity in the time series.

To investigate the possibility of multiple periodicities, we consider a multiparametric fit to the long-term evolution of the chromospheric activity of ι Hor. In this approach, we characterize each signal by a sinusoidal model, composed of three free parameters representing the period (P), semi-amplitude (A) and phase (Φ) of the modulation. While the entire time series is used in the analysis, an independent offset is calculated for data sets acquired with different instruments. Therefore, four[9] additional free parameters are included in our final model, corresponding to the mean activity levels $\langle S \rangle_{\rm SET}$ (compatible with the best-fitting model), associated with a particular data set or instrument.

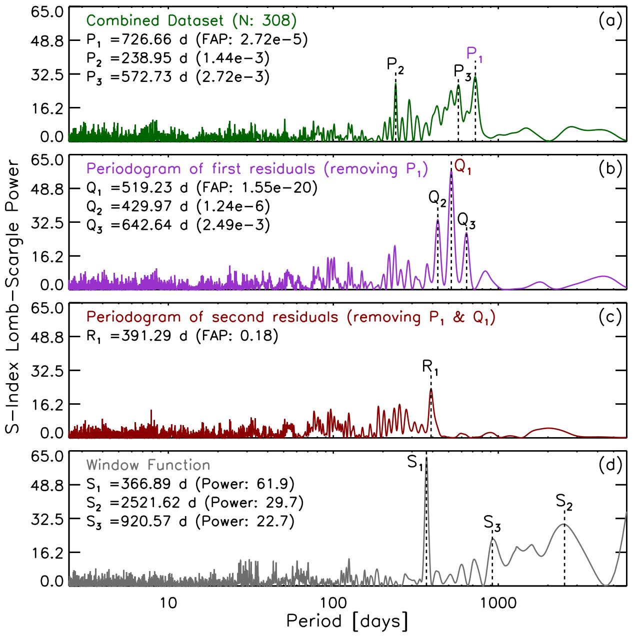

Figure 2. Results from periodicity analysis on the long-term S-index variations of ι Hor (Fig. 1). From top to bottom, Lomb–Scargle (LS) periodograms are presented for the original data set, the first and second residuals, and the window function.

We follow a sequential procedure to identify and extract the periodicities in a hierarchical manner. In this way, we consider the highest peak of the initial LS periodogram (P_1 in Fig. 2a), and

---

[9] For this treatment, we consider the HARPS PH3 and HARPSpol data sets independently.

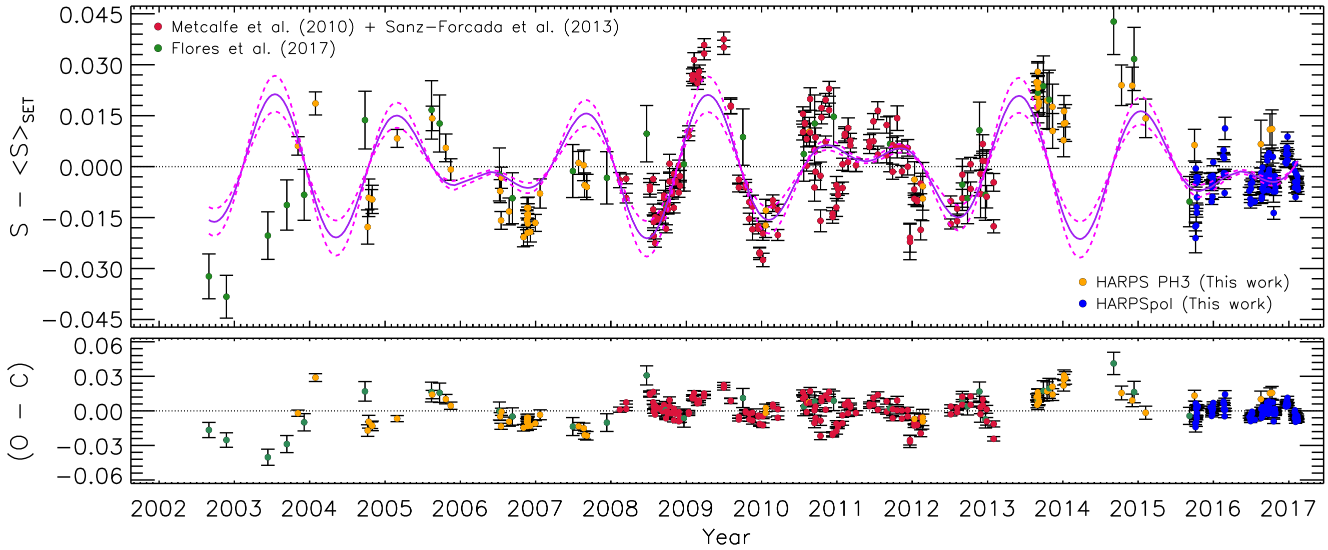

Figure 3. Results from the multiparametric fit to the activity cycle of ι Hor. The top panel contains the variation of the S-index relative to the mean value in each instrument ($S - \langle S\rangle_{\rm SET}$). The solid line corresponds to the best two-period model ($S_{\rm CYC}$), with $P_1 \simeq 1.97$ yr and $P_2 \simeq 1.41$ yr ($\chi_{\rm r}^2 = 16.73$). The dashed lines show the 3σ cycle amplitude limits, keeping the remaining parameters of the periodic signals fixed. The residuals are presented in the bottom panel.

obtain the best-fitting multiparametric model under a reduced $\chi_{\rm r}^2$ minimization scheme. This initial model is then subtracted from the original time series, from where an LS periodogram of the residuals is computed (Fig. 2b). The process is repeated for the highest peak in this new LS periodogram (Q_1 in Fig. 2b), which is then included in the multiparametric model and fitted simultaneously with the previously defined periodicity (therefore, the fitted parameters identified in the first step change slightly). Once again the best-fitting model (which now includes two periodic signals), is subtracted from the data and a second set of residuals is obtained. Similarly, an LS periodogram of the second residuals is generated (Fig. 2c), to check if there is any significant signal remaining in the data. As a consistency check, the best-fitting periods identified at every step in this process are compared against the location of the resulting peaks of the window function (Fig. 2d).

As presented in Fig. 2(c), the LS periodogram of second residuals yielded a peak at 391.29 d with an FAP = 0.18, which is not considered as significant and indicates the end of our iterative process. In this way, only two significant peaks were identified and for this reason, the multiparametric model considers two periodic signals (i.e. 10 free parameters). The final best-fitting solution ($S_{\rm CYC}$) is compared with the observations in Fig. 3, and a summary of the model is listed in Table 3. The errors have been estimated following a bootstrap resampling scheme (Press et al. 1992, 2002), generating 10^4 synthetic time series (randomly drawn from the original data set), and obtaining a best-fitting model for each one of them (the final model to the real data is used as an initial guess to accelerate the process). A 68 per cent confidence interval of the distribution resulting for each parameter of the synthetic fits is taken as the corresponding error in the final model.

As can be seen in Fig. 3, our model reproduces to a very good extent the long-term evolution of the chromospheric activity in the star. The overall behaviour clearly resembles a *beating* pattern, driven by the relatively small differences between the periods and amplitudes of the dominant signals (see Table 3). Note that none of the chromospheric cycle periods reported in the literature appear in our final solution. As explained below, these discrepancies were expected and can be explained by considering some differences between these previous studies and our analysis.

Table 3. Final two-period model ($S_{\rm CYC}$) for the activity evolution of ι Hor.

Parameter	Value
1st Component	
Period (P_1)	719 ± 7 d (1.968 ± 0.019 yr)
Semi-amplitude (A_1)	0.0118 ± 0.0010
Phase (Φ_1)	6.27 ± 0.16 rad
2nd Component	
Period (P_2)	516 ± 4 d (1.412 ± 0.010 yr)
Semi-amplitude (A_2)	0.0102 ± 0.0008
Phase (Φ_2)	4.51 ± 0.04 rad
Offsets $\langle S\rangle_{\rm SET}$	
REOSC (30)^a	0.233 ± 0.003
RC Spec (143)	0.2387 ± 0.0009
HARPS PH3 (60)	0.244 ± 0.002
HARPSpol (101)	0.2491 ± 0.0008
Statistics	
Reduced $\chi_{\rm r}^2$	16.73
Data points	334
$\langle S\rangle_{\rm ALL}$	0.24159 ± 0.00072

Note. ^{a}Number of data points for a given instrument.

As mentioned before, the 1.6-yr cycle was determined using observations acquired between 2008 and 2013 (Metcalfe et al. 2010; Sanz-Forcada et al. 2013), where good agreement was obtained towards the beginning and the end of this time span. However, this periodicity is unable to reproduce the entire ∼5-yr base line and is particularly inconsistent with the observed activity evolution between late-2010 and mid-2011. This is no longer the case in our approach, provided that all the observations are considered together and this particular data set puts very strong constraints during the fitting process since it provides the best cycle coverage of the entire time series. In addition, the apparent lack of coherence in the activity cycle observed between late-2010 and mid-2011 can now be understood in the framework of our model as simply the result of destructive interference between two, out of phase, periodic signals. Furthermore, the typical $\sim$5-yr[10] time-scale of this beating pattern can also explain the secondary cycle proposed by Flores et al. (2017), whose signal was probably enhanced by considering monthly averaged data (as was the case for their analysis).

As presented by different authors in the past, multiple chromospheric activity cycles are common among moderately active stars (e.g. Baliunas et al. 1995; Oláh et al. 2009, 2016), and most of these can be associated with the *active* and *inactive* sequences proposed by Brandenburg, Saar & Turpin (1998) and Böhm-Vitense (2007). In the latter form, each sequence is characterized by a roughly constant number of rotation periods per activity cycle (i.e. the ratio $P_{\mathrm{cyc}}/P_{\mathrm{rot}}$). For example, Egeland et al. (2015) report values of $n_{\mathrm{short}} \simeq 50$ and $n_{\mathrm{long}} \simeq 400$ (associated with the inactive and active branches, respectively), for the $\sim$1-Myr-old solar analogue HD 30495 (G1.5V, $P_{\mathrm{rot}} \simeq 11.36$ d, $P_{\mathrm{long}} \sim 12.2$ yr, $P_{\mathrm{short}} \sim 1.67$ yr). As discussed in Section 5.3, we obtain a $P_{\mathrm{rot}} \sim 7.7$ d for ι Hor which leads to $n_{\mathrm{short}} = P_2/P_{\mathrm{rot}} \simeq 67$ and $n_{\mathrm{long}} = P_1/P_{\mathrm{rot}} \simeq 93$. Given the relatively small n_{long} value of ι Hor compared to HD 30495, it might look that only the short cycle (P_2) could be associated with the inactive sequence. However, our n_{long} value is roughly consistent with the active branch at the location of the star in the cycle period versus rotation period diagram[11] of Böhm-Vitense (2007), as both sequences lie very close to each other in this region. This also explains why the ratio between the long and short cycle periods identified for ι Hor is smaller than for any other star with multiple periodicities (i.e. $P_1/P_2 \sim 1.39$). For comparison, from the set of stars with complex cycles reported by Oláh et al. (2016), the smallest[12] value of $P_{\mathrm{long}}/P_{\mathrm{short}}$ is 1.84 (HD131156B, K4V, $P_{\mathrm{rot}} \simeq 11.05$ d, $P_{\mathrm{long}} \sim 4.2$ yr, $P_{\mathrm{short}} \sim 2.28$ yr). Likewise from the compilation of stars with multiple cycle periods performed by Brandenburg, Mathur & Metcalfe (2017), a minimum value of $P_{\mathrm{long}}/P_{\mathrm{short}} = 1.73$ is found (HD 114710, F9V, $P_{\mathrm{rot}} \simeq 12.3$ d, $P_{\mathrm{long}} \sim 16.6$ yr, $P_{\mathrm{short}} \sim 9.6$ yr). The extreme location in the parameter space occupied by ι Hor motivates the importance of studying the evolution of its magnetic field, and how this field influences with the observed chromospheric and coronal activity.

In connection with the previous discussion, we present below two phenomenological scenarios which could lead to the observed behaviour in the chromospheric activity. For both cases, we consider as an additional constraint the information provided by the long-term X-ray monitoring of ι Hor (see Sanz-Forcada et al. 2013; Sanz-Forcada & Stelzer 2016; Stelzer 2017).

The first one takes elements from the solar case, assuming that the *real* activity cycle is $\sim$1.6 yr as identified in the X-ray observations (given the larger cycle contrast in this wavelength range; see Section 1). Our identified periods in the Ca H&K evolution could be then associated with a projection effect due to the $\sim 60^{\circ}$ inclination of the star,[13] (less important for the optically thin coronal emission) and a strong latitudinal migration of active regions. As has been shown in several Doppler-imaging studies of main-sequence and pre-main-sequence stars (see Strassmeier 2009), magnetically induced features (such as spots and faculae) seem to be concentrated towards the polar regions in very active stars, in contrast with the $\pm 30^{\circ}$ latitudinal belts of solar activity. As ι Hor does not reach the very high activity levels of these objects, but is certainly more active than the Sun, an intermediate situation is expected. In this way, an asymmetry could be induced in the temporal evolution of the *S*-index values, due to an uneven distribution (in space and time) of chromospherically active regions. More specifically, two signals with shorter and longer periods could be caused by the non-visibility, at certain times of the cycle,[14] of active regions from one hemisphere (located at latitudes larger than 60°), combined with the opposite situation (i.e. contributions from both hemispheres) as the cycle progresses and the active regions move towards the equator. A similar geometrical effect was previously proposed by Sanz-Forcada et al. (2013), where the change in the cycle period would be related with asymmetries in the emerging activity between the visible and the partially visible hemispheres.

The second scenario considers that the two periods extracted from our analysis of the *S*-index variations, belong to *independent activity cycles* (i.e. each one associated with a magnetic cycle). In this case, the X-ray emission should have contributions from *both* magnetic cycles, and therefore, the observed period in the coronal emission corresponds to an *apparent* mean value falling in between the two real magnetic cycle periods. This would also imply that, with sufficient time coverage and sampling, both chromospheric cycle periods should appear in the X-ray evolution, with a similar beating pattern governing the variability of the coronal activity. While there might be hints of a secondary cycle in the X-ray data (see Sanz-Forcada & Stelzer 2016), the available observations are still more consistent with a single 1.6-yr periodicity. Future monitoring of ι Hor in X-rays[15] may help to reveal if this second periodicity is present in the coronal variability of the star.

Finally, we would like to point out that these two scenarios should also imprint different signatures in the evolution of the magnetic field of the star. Assuming that the magnetic and activity time-scales are coupled as in the solar case, we expect a single polarity reversal over a period of 1.6 yr for the first-case scenario (i.e. a 3.2-yr magnetic cycle). The situation is more complicated for the second case, as a double magnetic cycle would allow additional evolution patterns to occur (some of them could significantly deviate from the solar behaviour). The ZDI reconstructions of the large-scale magnetic field of ι Hor, planned for the second paper of this study, could help us to establish if any of the previously discussed possibilities is occurring in the star.

5.2 ι Horologii b

We now evaluate the robustness of our HARPSpol RV values by comparing them against the expected variation due to the presence of ι Hor b. While an independent orbital solution could be obtained from our data, we use instead the parameters derived by Zechmeister et al. (2013), as these have been determined from a much larger baseline and a consistent treatment of data from several instruments (see Section 2). This also represents a more stringent approach, as we are not forcing a new best-fitting solution but rather comparing our results directly with the expected behaviour of the RV variations.

The SYSTEMIC 2 package (Meschiari et al. 2009) is used for this purpose, incorporating the HARPSpol RV values as an

---

[10] Formally, this comes from the inverse of the beating frequency $\nu_{\mathrm{beat}} = |\nu_1 - \nu_2| = \left|\frac{1}{P_1} - \frac{1}{P_2}\right| \simeq \left|\frac{1}{1.97} - \frac{1}{1.41}\right| \simeq 0.2\,\mathrm{yr}^{-1}$.

[11] See Metcalfe et al. (2016) for an updated version.

[12] We consider here the largest and smallest P_{cyc} values found by Oláh et al. (2016).

[13] Estimated by Metcalfe et al. (2010) assuming solid body rotation and previously reported values of $v\sin(i)$, R_* and P_{rot}.

[14] Following the solar analogy, this would occur near activity maximum.

[15] Additional observations with *XMM–Newton* are planned for the 2017–2018 period (AO 16, PI: Sanz-Forcada).

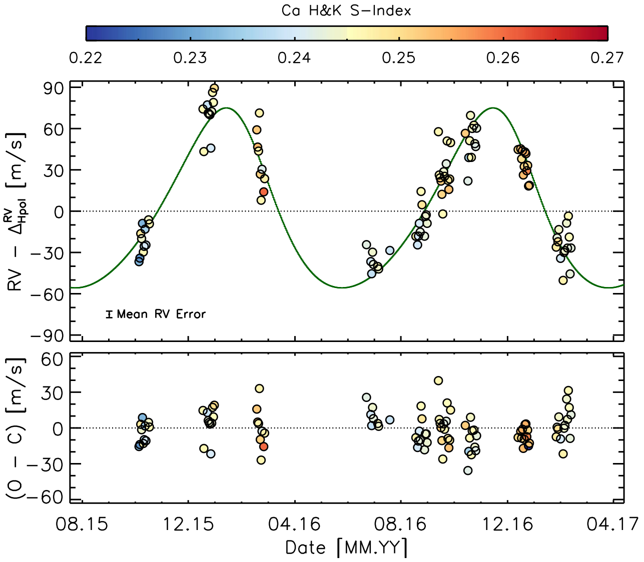

Figure 4. Evolution of the RV variations of ι Hor determined from the HARPSpol observations. The top panel shows the RV variation relative to a fixed instrumental offset (see the text for details). The solid line corresponds to the most recent orbital solution for ι Hor b (Zechmeister et al. 2013) and is used to compute the residuals in the bottom panel. Colours denote the associated Ca H&K *S*-index value for a given observation (Section 4.2).

independent data set and fixing all the orbital elements to the values provided by Zechmeister et al. (2013).[16] Only two parameters are fitted in this process, namely the periastron passage time (T_0 = 244 9738.248 15 d) and the RV reference level ($\Delta^{\mathrm{RV}}_{\mathrm{Hpol}}$ = 16 923.38 m s^{-1}), as it is necessary to adjust the phase (to include possible precession of the orbit with respect to our line of sight and the published solution) and the offset of the HARPSpol observations. The result shows very good agreement as illustrated in Fig. 4, where the residuals show an rms value of 13.52 m s^{-1} (slightly below the value reported by Zechmeister et al. 2013). This gives additional confidence to the RV values determined with the polarimetric mode of the HARPS spectrograph.

One important aspect to consider is the possible influence due to the evolving activity (measured in terms of the S_{H} and $I_{\mathrm{H}\alpha}$ indicators) and the longitudinal magnetic field (B_ℓ), over the RV variations of ι Hor. Following this idea, colours in Fig. 4 indicate the parallel evolution of the chromospheric activity of the star, given by the Ca H&K *S*-index. This comparison does not reveal any evident relation between the activity, the amplitude of the RV variations or the level of scatter of the residuals. However, we note that, while the nine HARPSpol epochs provide relatively good phase coverage of the exoplanet orbit (∼1.6 periods), their time-span falls short with respect to the activity cycle of the star (by ∼30 per cent), which displays epochs with considerably higher activity levels and variability (see Section 4.2, Fig. 1).

To improve this situation, we have expanded the baseline by including RV measurements from the HARPS PH3 observations (Section 3.2), extracted directly from the values reported by the pipeline.[17] As we are considering a single spectrum per night, we have assumed conservative limits for the RV uncertainties, taking three times the value listed in the final data products (corresponding to photon noise alone) and adding a typical 2.0 m s^{-1} error in quadrature. The combined HARPS PH3 and HARPSpol RV results are presented in Fig. 5, which have been now phase-folded to the orbital period of the exoplanet and include the evolution of the Ca H&K S-index (*left*) and the H α-index (*middle*). The *right*-hand panel of Fig. 5 contains a similar plot for the corresponding surface-average longitudinal magnetic field values (B_ℓ), only available for our HARPSpol observations.

There are some elements of Fig. 5 that are noteworthy. First of all, it is clear that the large variations of the RV of ι Hor are associated with a substellar companion, and not with the ongoing activity–magnetic cycle. This can be seen from the fact that RV values consistent with the exoplanet orbit have been observed at nearly all phases which display, at the same time, the full extent of activity levels in the star (Fig. 5, *left-hand* and *middle panels*). Likewise, as discussed in the Sun-as-a-star study performed by Haywood et al. (2016), RV variations due to activity features show a strong correlation with the corresponding disc-averaged magnetic flux density. As this quantity should be proportional (to a first order) to the longitudinal magnetic field, the lack of coherence between the B_ℓ evolution and the RV signal (Fig. 5, *right*), further supports a non-magnetic origin for the observed long-term RV variations of ι Hor.

On the other hand, an *activity gradient* appears around the exoplanet orbit in the *left-* and *right-hand* panels of Fig. 5. Assuming that the solution obtained by Zechmeister et al. (2013) is a good representation of the system, this suggests that the activity level dominates the structure of the RV residuals. In this way, the RV measurements obtained during epochs of low activity are systematically lower compared with the expected values, whilst the opposite situation occurs for epochs of high activity. A similar pattern has been previously reported for the less active solar twin HIP 11915 (Bedell et al. 2015), and considered as a signature of convective blueshift suppression by localized magnetic fields. Determining how such behaviour could be modelled and removed from the observations is out of the scope of this paper. Nevertheless, such an investigation would clearly be of value for understanding stellar activity and its contribution as noise to RV planet searches.

5.3 Rotation period

The last part of our analysis involves the short-term variability and the determination of the rotation period of the star (P_{rot}). Literature values of this parameter range between 7.9 d (Saar & Osten 1997) and 8.5 d (Metcalfe et al. 2010). The former estimate was obtained from the level of chromospheric emission (expressed in the form of the R'_{HK} indicator), and the empirical period–activity relation from Noyes et al. (1984). The latter considered an LS periodicity analysis from a time series of chromospheric Ca H&K *S*-index values (between early-2008 and mid-2010 in Fig. 1). In addition, similar P_{rot} values were inferred by Boisse et al. (2011), using LS analysis over simulated activity signals in order to fit the short-term RV variations of the star (determined from short-cadence HARPS data).

Here, we follow a combined approach, incorporating in the LS analysis the evolution of the Ca H&K *S*-index, the RV variations and the longitudinal magnetic field. As the activity cycle and the exoplanet signals are dominant in the former two cases, it is necessary to remove their contribution to extract any short-term periodicity from the data. This step has been carried out in order to produce the LS periodograms shown in Figs 6(a) and (b), removing, respectively,

---

[16] This includes a stellar mass for ι Hor of $M_* = 1.25\ \mathrm{M}_\odot$.

[17] http://www.eso.org/rm/api/v1/public/releaseDescriptions/72

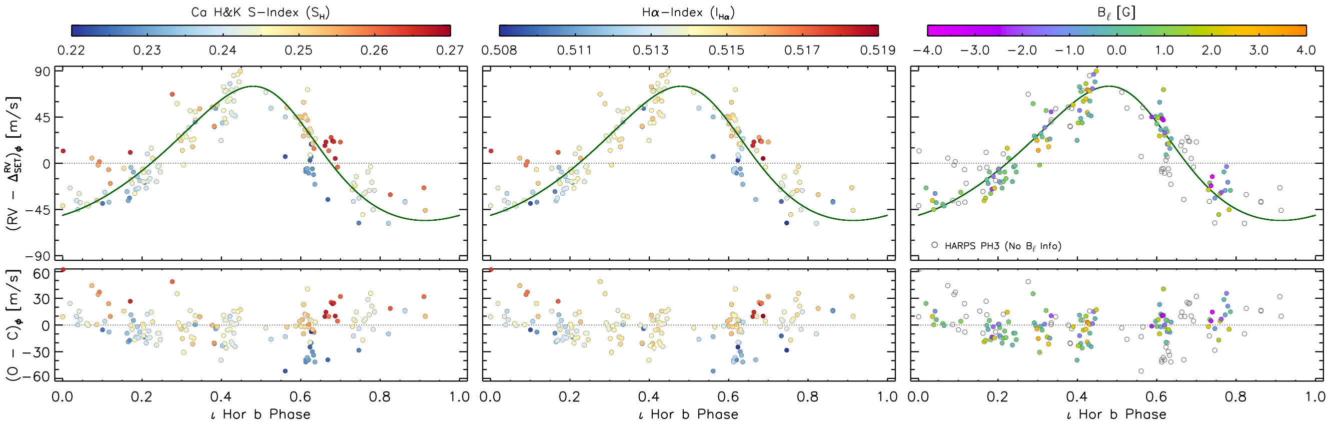

Figure 5. RV variations of ι Hor determined from the combined HARPS PH3 and HARPSpol data sets. The phase and orbital solution (solid line) have been calculated using the parameters reported by Zechmeister et al. (2013). The colour bars denote the corresponding values of $S_{\rm H}$ (left), $I_{{\rm H}\alpha}$ (middle) and B_ℓ (right) for each observation. The residuals are shown in the bottom panel.

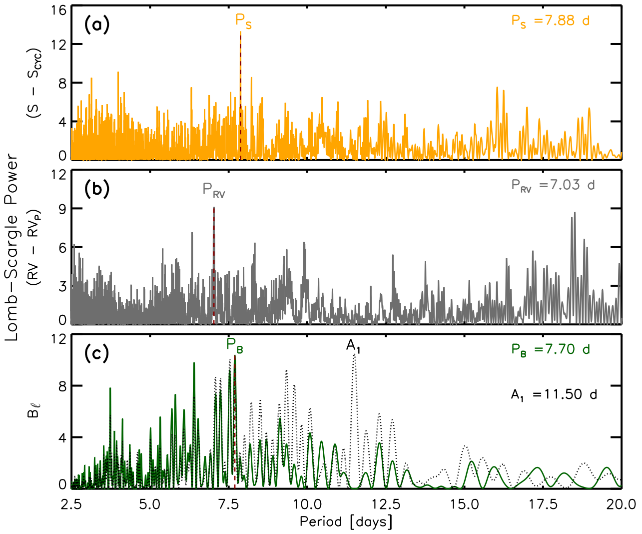

Figure 6. Estimation of the rotation period ($P_{\rm rot}$) of ι Hor. Each panel contains the LS periodogram associated with the short-term variability of a specific parameter. After the removal of the dominant cycle ($S_{\rm cyc}$) and exoplanet (RV$_{\rm p}$) signals, the residual activity and RV variations are considered for panels a and b, respectively. The time series of B_ℓ measurements listed in Table 2 are used to derive the raw (dotted line) and final (solid line) LS periodograms of panel c (see the text for more details). The identified period is indicated in each case.

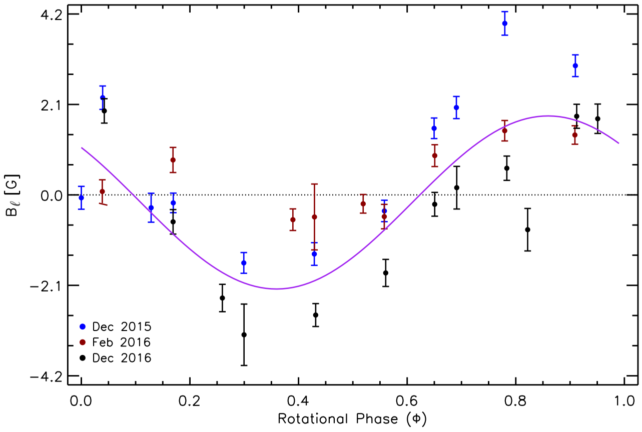

Figure 7. Evolution of the longitudinal magnetic field of ι Hor as a function of rotational phase (with $P_{\rm rot} = 7.7$ d). Three separate epochs are presented, whose reference $\phi = 0$ dates have been adjusted individually. The solid line (not a fit) shows a phased 7.7-d period sine curve as reference.

our best-fitting two-period activity cycle model ($S_{\rm CYC}$, Section 4.2) and the exoplanet RV signature (RV$_{\rm p}$, Section 5.2[18]). Fig. 6(c) shows the results derived from our series of B_ℓ measurements (Table 2). A raw LS periodogram of the data (dotted line) shows two prominent peaks located at 11.50 d and 7.70 d with nearly the same amplitude. However, as can be seen in Figs 6(a) and (b), the former peak does not appear in the LS periodograms of the chromospheric activity or the RVs. In addition, an 11.50 d period would not only strongly disagree with the reports discussed in the previous paragraph, but also would be incompatible with the level of coronal emission observed in this star (see Pizzolato et al. 2003; Sanz-Forcada et al. 2013). Furthermore, this longer rotation period would be inconsistent with the allowed values from solid body rotation and published values of R_* and $v\,\sin(i)$, including uncertainties (see Table 1).[19] For these reasons, we interpret this period as a possible artefact which could be related to our data sampling (as most of our epochs are composed of 11 observations). The removal of this signal yields the final LS periodogram from this time series (solid line in Fig. 6c).

Given the low significance of the identified peaks in all cases and the relatively clearer signal obtained from the B_ℓ data set (even with much fewer data points), we take the 7.7 d as the rotation period of the star and use the other two values as conservative limits for the uncertainty. Additionally, as illustrated in Fig. 7, this value appears directly by looking at the evolution of B_ℓ in certain epochs, which is not the case for any of the activity proxies or the RV variations. This corroborates the findings of Hébrard et al. (2016), which showed that time series of B_ℓ measurements provide a more robust signature

---

[18] The removed signal was slightly different from the one presented in Section 5.2. The formal best-fitting orbital solution was used in this case ($P_{\rm orb} \simeq 308.3$ d, $M_{\rm p}\sin(i) \simeq 2.27$ M$_{\rm J}$, $e \simeq 0.16$, $\omega \simeq 64.^{\circ}3$), as required for a consistent extraction of the rotation period. The RV offsets (for HARPS and HARPSpol) and the T_0 value were kept fixed with respect to the values used in Section 5.2.

[19] This means $\sin i = (P_{\rm rot} \cdot v\,\sin i)/(2\pi R_*) > 1.0$.

for the determination of $P_{\rm rot}$ compared to other activity indicators or the RVs.

6 SUMMARY

We presented here the initial results of our long-term monitoring campaign of ι Hor using the spectropolarimetric capabilities of the HARPS spectrograph. This paper explored the different time-scales of variability on the magnetic activity and RV of the star, and provided information concerning the observing strategy and the data reduction process. Measurements of the surface-averaged longitudinal magnetic field of this object are also reported here for the first time. The observed range of variability for this parameter (±4 G) is fully consistent with the scatter reported in snapshot observations of stars of similar spectral type and age (Marsden et al. 2014).

Our analysis revisited the activity cycle of ι Hor, showing that the long-term evolution of the chromospheric activity can be fairly reproduced by a beating pattern, resulting from the superposition of two, out-of-phase, periodic signals of similar amplitude (Section 5.1). The identified periods and their corresponding amplitudes are $P_1 \simeq 1.97 \pm 0.02$ yr with $A_1 = 0.0118 \pm 0.0010$ and $P_2 \simeq 1.41 \pm 0.01$ yr with $A_2 = 0.0102 \pm 0.0008$. Two different physical scenarios were proposed and discussed in order to place this particular behaviour in the general solar-stellar context.

We also presented here 101 new RV measurements of ι Hor, which showed a remarkably good agreement with the expected evolution due to the presence of the exoplanet of this system (Section 5.2). By simultaneously tracing the evolution of the magnetic activity and the RV, we find evidence of the former controlling the structure of the residual variations in the latter (once the signal from the exoplanet has been removed). While this poses a challenge in the search for additional planets in this system, characterizing this behaviour in a larger sample of active planet-hosting stars could represent a step forward in our understanding of stellar activity in the exoplanet context.

Finally, we estimated here a rotation period for ι Hor of ~7.7 d, roughly in agreement with the lower end of previous reports in the literature (Section 5.3). This value is likely to be improved using the information contained in the shapes of the LSD Stokes *V* profiles, and the optimization routines applied during the ZDI analysis planned for a future study.

ACKNOWLEDGEMENTS

We would like to thank the referee, Martin Kürster, for his constructive comments which helped to improve the quality of this paper. JDAG was supported by *Chandra* grants AR4-15000X and GO5-16021X. JJD was supported by NASA contract NAS8-03060 to the *Chandra* X-ray Center. JSF acknowledges support from the Spanish MINECO through grant AYA2014-54348-C3-2-R. Support for OC and SPM is provided by NASA Astrobiology Institute grant NNX15AE05G. CG was supported by *HST* GO-13754 and *Chandra* GO7-18017X grants. This work is based on observations collected at the European Organisation for Astronomical Research in the Southern hemisphere under ESO programmes 096.D-0257, 097.D-0420 and 098.D-0187. We are thankful to the different ESO OPC reviewers for the allocation of the HARPSpol observing time in each semester, and with the ESO OPO for accommodating the required observing strategy for this project. JDAG would also like to thank the staff of the ESO La Silla Observatory for the strong support during each observing run of this programme. This work is also based on data obtained from the ESO Science Archive Facility under request number jalvarad.212739. This work has made use of the VALD data base, operated at Uppsala University, the Institute of Astronomy RAS in Moscow and the University of Vienna. This research has made use of the SIMBAD data base, operated at CDS, Strasbourg, France. This research has also made use of NASA's Astrophysics Data System.

REFERENCES

Alvarado-Gómez J. D. et al., 2015, A&A, 582, A38
Aschwanden M. J., 1994, Sol. Phys., 152, 53
Ayres T. R., 2009, ApJ, 696, 1931
Ayres T. R., 2014, AJ, 147, 59
Ayres T. R., Judge P. G., Saar S. H., Schmitt J. H. M. M., 2008, ApJ, 678, L121
Bagnulo S., Landolfi M., Landstreet J. D., Landi Degl'Innocenti E., Fossati L., Sterzik M., 2009, PASP, 121, 993
Baliunas S. L. et al., 1995, ApJ, 438, 269
Barnes S. A., 2007, ApJ, 669, 1167
Bazilevskaya G., Broomhall A.-M., Elsworth Y., Nakariakov V. M., 2014, Space Sci. Rev., 186, 359
Bedell M. et al., 2015, A&A, 581, A34
Bieber J. W., Seckel D., Stanev T., Steigman G., 1990, Nature, 348, 407
Blanco-Cuaresma S., Soubiran C., Jofré P., Heiter U., 2014a, A&A, 566, A98
Blanco-Cuaresma S., Soubiran C., Heiter U., Jofré P., 2014b, A&A, 569, A111
Böhm-Vitense E., 2007, ApJ, 657, 486
Boisse I., Bouchy F., Hébrard G., Bonfils X., Santos N., Vauclair S., 2011, A&A, 528, A4
Bonfils X. et al., 2007, A&A, 474, 293
Boro Saikia S. et al., 2016, A&A, 594, A29
Brandenburg A., Saar S. H., Turpin C. R., 1998, ApJ, 498, L51
Brandenburg A., Mathur S., Metcalfe T. S., 2017, ApJ, 845, 79
Bruntt H. et al., 2010, MNRAS, 405, 1907
Butler R. P., Tinney C. G., Marcy G. W., Jones H. R. A., Penny A. J., Apps K., 2001, ApJ, 555, 410
Butler R. P. et al., 2006, ApJ, 646, 505
DeWarf L. E., Datin K. M., Guinan E. F., 2010, ApJ, 722, 343
Diego F., Charalambous A., Fish A. C., Walker D. D., 1990, in Crawford D. L., ed., Proc. SPIE Conf. Ser. Vol. 1235, Instrumentation in Astronomy VII. SPIE, Bellingham, p. 562
Donati J.-F., Landstreet J. D., 2009, ARA&A, 47, 333
Donati J.-F., Semel M., Carter B. D., Rees D. E., Collier Cameron A., 1997, MNRAS, 291, 658
Egeland R., Metcalfe T. S., Hall J. C., Henry G. W., 2015, ApJ, 812, 12
Egeland R., Soon W., Baliunas S., Hall J. C., Pevtsov A. A., Henry G. W., 2016, in Feiden G., ed., the 19th Cambridge Workshop on Cool Stars, Stellar Systems, and the Sun (CS19). Zenodo, 6
Egeland R., Soon W., Baliunas S., Hall J. C., Pevtsov A. A., Bertello L., 2017, ApJ, 835, 25
Fares R., 2016, IAU Focus Meeting, 29, 360
Favata F., Micela G., Baliunas S. L., Schmitt J. H. M. M., Güdel M., Harnden F. R., Jr, Sciortino S., Stern R. A., 2004, A&A, 418, L13
Favata F., Micela G., Orlando S., Schmitt J. H. M. M., Sciortino S., Hall J., 2008, A&A, 490, 1121
Flores M. G., Buccino A. P., Saffe C. E., Mauas P. J. D., 2017, MNRAS, 464, 4299
Gizis J. E., Reid I. N., Hawley S. L., 2002, AJ, 123, 3356
Hall J. C., Lockwood G. W., Skiff B. A., 2007, AJ, 133, 862
Hall J. C., Henry G. W., Lockwood G. W., Skiff B. A., Saar S. H., 2009, AJ, 138, 312
Hathaway D. H., 2015, Living Rev. Sol. Phys., 12, 4
Haywood R. D. et al., 2016, MNRAS, 457, 3637
Hébrard É. M., Donati J.-F., Delfosse X., Morin J., Moutou C., Boisse I., 2016, MNRAS, 461, 1465

Hempelmann A., Robrade J., Schmitt J. H. M. M., Favata F., Baliunas S. L., Hall J. C., 2006, A&A, 460, 261

Henry T. J., Soderblom D. R., Donahue R. A., Baliunas S. L., 1996, AJ, 111, 439

Horne J. H., Baliunas S. L., 1986, ApJ, 302, 757

Hussain G. A. J. et al., 2009, MNRAS, 398, 189

Hussain G. A. J. et al., 2016, A&A, 585, A77

Judge P. G., Solomon S. C., Ayres T. R., 2003, ApJ, 593, 534

Katsova M. M., Bondar N. I., Livshits M. A., 2015, Astron. Rep., 59, 726

Kochukhov O., Makaganiuk V., Piskunov N., 2010, A&A, 524, A5

Kupka F. G., Ryabchikova T. A., Piskunov N. E., Stempels H. C., Weiss W. W., 2000, Balt. Astron., 9, 590

Kürster M., Endl M., Els S., Hatzes A. P., Cochran W. D., Döbereiner S., Dennerl K., 2000, A&A, 353, L33

Kürster M. et al., 2003, A&A, 403, 1077

Laymand M., Vauclair S., 2007, A&A, 463, 657

Lomb N. R., 1976, Ap&SS, 39, 447

Lovis C., Fischer D., 2010, Radial Velocity Techniques for Exoplanets. Univ. Arizona Press, Tucson, AZ, p. 27

McIntosh S. W. et al., 2015, Nat. Commun., 6, 6491

Mackay D. H., Yeates A. R., 2012, Living Rev. Sol. Phys., 9, 6

Marsden S. C. et al., 2014, MNRAS, 444, 3517

Mauas P. J. D. et al., 2012, in Mandrini C. H., Webb D. F., eds, Proc. IAU Symp. 286, Comparative Magnetic Minima: Characterizing Quiet Times in the Sun and Stars. Cambridge Univ. Press, Cambridge, p. 317

Mayor M. et al., 2003, The Messenger, 114, 20

Meschiari S., Wolf A. S., Rivera E., Laughlin G., Vogt S., Butler P., 2009, PASP, 121, 1016

Metcalfe T. S., Basu S., Henry T. J., Soderblom D. R., Judge P. G., Knölker M., Mathur S., Rempel M., 2010, ApJ, 723, L213

Metcalfe T. S., Egeland R., van Saders J., 2016, ApJ, 826, L2

Montes D., López-Santiago J., Gálvez M. C., Fernández-Figueroa M. J., De Castro E., Cornide M., 2001, MNRAS, 328, 45

Naef D., Mayor M., Pepe F., Queloz D., Santos N. C., Udry S., Burnet M., 2001, A&A, 375, 205

Nordström B. et al., 2004, A&A, 418, 989

Noyes R. W., Hartmann L. W., Baliunas S. L., Duncan D. K., Vaughan A. H., 1984, ApJ, 279, 763

Oláh K. et al., 2009, A&A, 501, 703

Oláh K., Kővári Z., Petrovay K., Soon W., Baliunas S., Kolláth Z., Vida K., 2016, A&A, 590, A133

Orlando S., Peres G., Reale F., 2001, ApJ, 560, 499

Piskunov N., Kochukhov O., 2002, A&A, 381, 736

Piskunov N. et al., 2011, =The Messenger, 143, 7

Pizzolato N., Maggio A., Micela G., Sciortino S., Ventura P., 2003, A&A, 397, 147

Press W. H., Teukolsky S. A., Vetterling W. T., Flannery B. P., 1992, Numerical Recipes in C. The Art of Scientific Computing. Cambridge Univ. Press, Cambridge

Press W. H., Teukolsky S. A., Vetterling W. T., Flannery B. P., 2002, Numerical Recipes in C++: The Art of Scientific Computing. STScI, Baltimore

Robrade J., Schmitt J. H. M. M., Favata F., 2012, A&A, 543, A84

Rosén L., Kochukhov O., Wade G. A., 2015, ApJ, 805, 169

Ryabchikova T., Piskunov N., Kurucz R. L., Stempels H. C., Heiter U., Pakhomov Y., Barklem P. S., 2015, Phys. Scr., 90, 054005

Saar S. H., Brandenburg A., 1999, ApJ, 524, 295

Saar S. H., Osten R. A., 1997, MNRAS, 284, 803

Sanz-Forcada J., Stelzer B., 2016, in Feiden G., ed., 19th Cambridge Workshop on Cool Stars, Stellar Systems, and the Sun (CS19). Zenodo, p. 112

Sanz-Forcada J., Micela G., Ribas I., Pollock A. M. T., Eiroa C., Velasco A., Solano E., García-Álvarez D., 2011, A&A, 532, A6

Sanz-Forcada J., Stelzer B., Metcalfe T. S., 2013, A&A, 553, L6

Scargle J. D., 1982, ApJ, 263, 835

See V. et al., 2016, MNRAS, 462, 4442

Skumanich A., 1972, ApJ, 171, 565

Stelzer B., 2017, Astron. Nachr., 338, 195

Strassmeier K. G., 2009, A&AR, 17, 251

Suárez Mascareño A., Rebolo R., González Hernández J. I., 2016, A&A, 595, A12

Valenti J. A., Fischer D. A., 2005, ApJS, 159, 141

van Leeuwen F., 2007, A&A, 474, 653

Vauclair S., Laymand M., Bouchy F., Vauclair G., Hui Bon Hoa A., Charpinet S., Bazot M., 2008, A&A, 482, L5

Vaughan A. H., Preston G. W., 1980, PASP, 92, 385

Wargelin B. J., Saar S. H., Pojmański G., Drake J. J., Kashyap V. L., 2017, MNRAS, 464, 3281

Wilson O. C., 1968, ApJ, 153, 221

Zechmeister M. et al., 2013, A&A, 552, A78

This paper has been typeset from a TEX/LATEX file prepared by the author.